A Nonparametric estimator for Coherent Change Detection: the Permutational Change Detection

Giovanni Costa [iD] , Andrea Virgilio Monti-Guarnieri [iD] , *Senior Member, IEEE,* Marco Manzoni [iD] , *Member, IEEE* and Alessio Rucci

Abstract—Nowadays, Synthetic Aperture Radar (SAR) is widely used in heterogeneous fields with aims strictly dependent on the objectives of the application. One of the most common is the exploitation of the Interferometric-SAR (InSAR) to measure millimeter movements on the Earth's surface, aiming to monitor failures (e.g. landslides) or to measure the health state of infrastructures (e.g. mining assets, bridges, buildings, etc). In this context, developing algorithms to detect temporal and spatial changes in the radar targets becomes very important. This paper focuses on the temporal change detection framework, proposing a nonparametric Coherent Change Detection (CCD) algorithm called Permutational Change Detection (PCD), a purely statistical algorithm whose core is the Permutation Test. The PCD estimates the temporal Change Points (CPs) of a radar target recognizing *blocks structure* in the coherence matrix, namely new radar objects. The algorithm has been fine-tuned for small SAR datasets, with the specific aim of prioritizing the analysis of the latest changes. A rigorous mathematical derivation of the algorithm is carried out, explaining how some limits have been addressed. Then, the performance analysis on simulated data is deeply accomplished, carried out for the stand-alone PCD and for the PCD compared with a parametric CCD algorithm based on the Generalized Likelihood Ratio Test (GLRT), and with the Omnibus and REACTIV detectors. The comparison with these other algorithms and the stand-alone performance analysis point out the robustness of the PCD in dealing with very noisy environments, even in the case of a single block. Finally, the PCD is validated by processing two Sentinel I data stacks, ascending and descending geometry, of the 2016 Central Italy earthquake.

Index Terms—SAR, InSAR, Nonparametric Coherent Change Detection, Change Points, Blocks structure, Permutation Tests.

I. INTRODUCTION

OVER the last two decades, Synthetic Aperture Radar (SAR) has been used successfully for the study of surface deformation phenomena (e.g. landslides, subsidence, sinkholes) and for monitoring various assets and infrastructures (e.g. pipelines, bridges) by applying interferometric techniques (InSAR) to long temporal series of radar images acquired over the same area of interest. The main idea of these techniques is to identify a set of coherent points on the ground showing a stable radar return with time, along all the temporal window of the analysis, and extract displacement information exploiting all SAR images in the data stack. Radar targets can be point-wise, generally corresponding to man-made objects

Giovanni Costa, Andrea Virgilio Monti-Guarnieri and Marco Manzoni are with the Dipartimento di Elettronica, Informazione e Bioingegneria, Politecnico di Milano, 20133 Milan, Italy (e-mail:giovanni.costa@polimi.it).
Alessio Rucci is with TRE ALTAMIRA s.r.l., 20143 Milan, Italy.
Manuscript received April 19, 2005; revised September 17, 2014.

called Permanent Scatterers (PS) [1] [2] [3] widely available in urban areas but also Distributed Scatterers (DS) [4], present mainly in non-urban areas. The SqueeSAR approach [4] jointly processes PS and DS, considering the different statistical behavior of each measurement point and properly combining the information associated with all possible interferograms that can be computed based on the InSAR data stack under study. The main limitation of the algorithms used today is their difficulty in dealing with changes in the scenario under analysis. Coherent points, whether PS or DS, can change in time, sometimes disappearing [5] [6], and new measurement points can become available (e.g., a new suburb in a city). The location and the time of severe changes affecting the area of interest are per se information: it should be provided to final users, complementing any InSAR analysis. The detection of the changes is carried out by the analysis of the time series, for point-wise PS targets, but also by studying the coherence (or covariance) matrix of all DS, which is a complete description of the statistical behavior of the radar target, at least for Gaussian scatterers. Identifying a blocks structure of this matrix can allow users to immediately detect the presence of changes and possibly different objects in different periods. The modeling of the coherence values of each block of the matrix – if not corresponding to a fully decorrelated area - can then provide valuable information for characterizing each object. It should be noted that severe changes in the coherence values of a PS or DS do not always correspond to the presence of different objects. For instance, snow coverage over mountainous areas can prevent any useful InSAR analysis during the winter period, but SAR images acquired after the snow melts can still exhibit a decent coherence when correlated with those acquired before the snow period. In this framework, several algorithms were developed exploiting the amplitude [7] [8] [9] or the phase [10] [11] [12] [13] of the acquired signals. The main difference is that the Amplitude Change Detection algorithms (ACD) compare the intensity of two radar images, looking for significant changes in the backscatter of the targets. Instead, the Coherent Change Detection algorithms (CCD) compare the radar images through their phase by exploiting the coherence between the acquisitions. CCD is far more sensitive because the phase is measured to within a small fraction of the wavelength and can be used to detect subtle changes that would remain undetected by following ACD approaches. Even if CCD is more sensitive, its applicability is limited by vegetation cover or, generally, by areas that are often decorrelated.

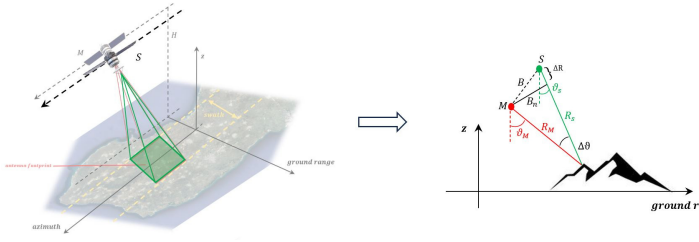The method here proposed moves in the CCD framework,

Fig. 1. Across-track SAR interferometer. On the left, the 3D figure simulates the slave acquisition in the same geometry shown in Figure 2. On the right, the cross-section along the across-track plane.

aiming to detect severe changes looking if the coherence matrix of the radar target presents blocks structure, without any assumptions on the number of changes as well as the extension of the blocks. Moreover, it can deal with non-stationary decorrelation phenomena affecting the analyzed target, which is typical of a real scenario. The algorithm is detailed in Section II after a theoretical introduction about the adopted models and mathematical tools. A deep performance analysis on simulated data is carried out in Section VI, and in Section VII the PCD is also compared with the parametric CCD algorithm proposed in [10], and with the two SAR change detection techniques proposed in [14], [15] and [16]. Finally, in Section VIII the Central Italy earthquake of August 2016 is taken as a case study to validate the algorithm. In the last section, conclusions are drawn.

II. PERMUTATIONAL CHANGE DETECTION (PCD)

The *Permutational Change Detection* (PCD) is a nonparametric CCD algorithm that estimates changes in coherence of a radar target identifying blocks in the coherence matrix $\hat{\Gamma}$. It consists of two steps:

- *Change Point Detection* (CPD): detection of the *candidate change point* (C-CP);
- *Change Point Validation* (CPV): validation of the candidate;

and gives as outputs:

- *Change Detection Matrix* (CDM): a matrix of the same dimension of $\hat{\Gamma}$ showing the estimated model for the pixel under analysis;
- *Change Vectors* (CV): vectors of length equal to the dimension of the dataset, storing the temporal location of the changes;

To better understand the mathematical details of the PCD steps (Section III and IV), an overview of the most important theoretical concepts is carried out in Section II-A.

A. Coherence Matrix, Block Model and Permutation Tests

1) Coherence Matrix: Given a SAR data stack of NI images, for each pixel, $\hat{\Gamma}$ is the $[NI, NI]$ matrix containing the modulus of the interferometric coherence [17] $\hat{\gamma}_{ij}$ between
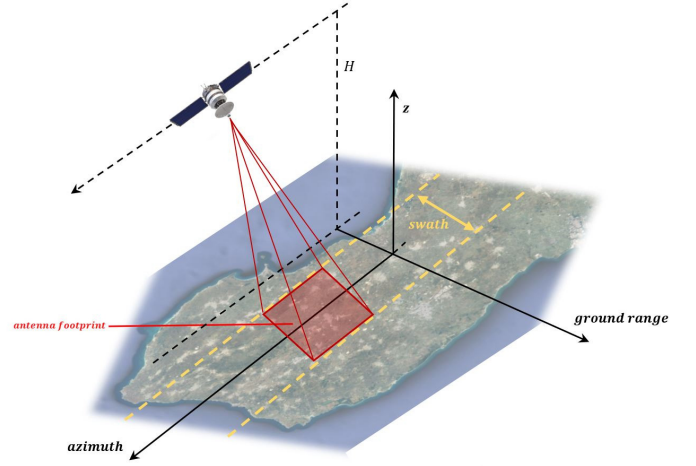

Fig. 2. SAR imaging geometry.

the i_{th} and j_{th} image, estimated over a window of dimension L, number of looks. In formulas

$$\hat{\Gamma} = \frac{1}{L} \left| \frac{\sum_{l=1}^{L} y(l) y^H(l)}{\sqrt{\sum_{l=1}^{L} |y(l)|^2 |y^H(l)|^2}} \right|, \qquad (1)$$

where $\mathbf{y}(l) \in \mathbb{C}^{NI}$ is the vector collecting the temporal samples of the l-th pixel. Each sample of $\hat{\Gamma}$ depends on the differences in the acquisition time and position of the sensors, and other noisy sources. Figure 1 shows the geometry of two generic acquisitions: we denote as *temporal baseline* B_t the difference in days between the primary (*M*) and secondary acquisition (*S*), instead the *geometrical baseline* B is the distance between *M* and *S* in the plane perpendicular to the orbit of the primary. Finally, its perpendicular projection on the slave *line of sight* is called *normal baseline*. B_n.

Herewith we will account for the following coherence contributions [17] [18] [19] [20] [21] [22]:

$$\hat{\Gamma} \simeq \gamma_0 \gamma_t \gamma_b \gamma_n, \qquad (2)$$

where

- γ_0: maximum theoretical coherence;
- $\gamma_t = e^{-\frac{|B_{t_{ij}}|}{\tau}}$: temporal decorrelation with time constant τ [18] [19];
- $\gamma_b = \left(1 - \frac{B_{n_{ij}}}{B_c}\right)$: geometric decorrelation with B_c *critical baseline* [23];
- γ_n: other noise sources.

The exponential model for the temporal decorrelation γ_t, has been widely adopted for vegetated targets [18].

Concerning the noise model, for simplicity is assumed to be distributed like a Rayleigh [24] with scale parameter $\sqrt{\frac{1}{2L}}$ (Section III and IV).

2) Block Model: The paper investigates changes implying significant alteration of the backscatter properties, such that a target can evolve into new objects. Figure 3 shows simple examples of changes we are interested in, associating plausible coherence matrices describing the behavior of the temporal evolution of the scatterers. Consider the target within the
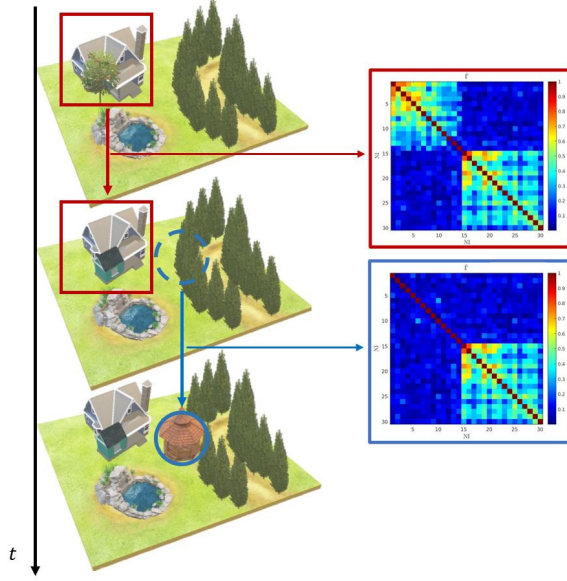
Fig. 3. Examples of target changes described by plausible coherence matrices.
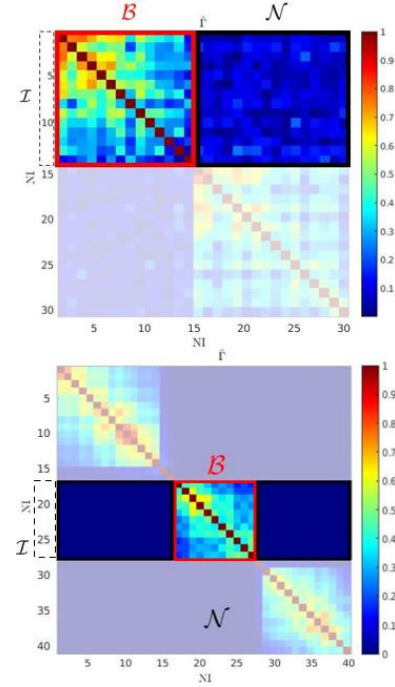

Fig. 4. Example of blocks structures. The red and black squares indicate the block $\mathcal{B}$ and $\mathcal{N}$, respectively. The black dashed line defines the group of images $\mathcal{I}$.

blue circle, where coherence is enhanced by replacing trees with a marquee. Conversely, the target within the red square undergoes a change due to the addition of a new room to the house. In this scenario, the target doesn't lose coherence but evolves into a new object from a radar point of view. We referred to targets gaining or losing coherence, or both, respectively as *Temporary Coherent Scatterers (TCS)* or *Semi Permanent Scatterers (SPS)* [25].

Whenever a new radar object is born, $\hat{\Gamma}$ presents *blocks structure* (Figure 4), implying that the change is not reversible. *Not reversible* underlines the difference in cases where the coherence changes are temporary, and the same electromagnetic features can be recovered, i.e., snow periods. Mathematically, a block $\mathcal{B}$ is a square submatrix of $\hat{\Gamma}$ determined by a group of consecutive coherence estimates much greater than the ones outside the block. In formulas by using the set theory notations, being

$$\mathcal{D} = \{1, 2, ..., NI\}, \tag{3}$$

the set of the indexes of the observations, and

$$\mathcal{I} = \left\{ i \in \mathcal{D} \,\middle|\, \hat{\gamma}_{ij} > \epsilon \,\forall j \in \mathcal{D} \text{ and } j \neq i \right\}, \tag{4}$$

the groups of indexes of the observations satisfying the condition above, then

$$\mathcal{B} = \{\hat{\gamma}_{ij} \in \hat{\Gamma} \,|\, i, j \in \mathcal{I}\}, \tag{5}$$

and the relative noise block is

$$\mathcal{N} = \{\hat{\gamma}_{ij} \in \hat{\Gamma} \,|\, i \in \mathcal{I}, j \in \mathcal{D} \setminus \mathcal{I}\} = \mathcal{B}^c, \tag{6}$$

where ^{c} indicates the complement operation.

Under these conditions, it is possible to write the $ij - th$ element of $\hat{\Gamma}$ as

$$\hat{\gamma}_{ij} = \frac{1}{L} \left| \frac{\sum_{l=1}^{L} y_i(l) y_j^H(l)}{\sqrt{\sum_{l=1}^{L} |y_i(l)|^2 |y_j^H(l)|^2}} \right| \simeq \gamma_{\mathcal{B}_{ij}} \gamma_{t_{ij}} \gamma_{b_{ij}} \gamma_{n_{ij}}, \tag{7}$$

where $\gamma_{\mathcal{B}_{ij}}$ is the $ij - th$ element of the block model of $\hat{\Gamma}$, which can be theoretically modelled as

$$\gamma_{\mathcal{B}_{ij}} = \begin{cases} 1 & \text{if } i, j \in \mathcal{I}, \\ 0 & \text{otherwise.} \end{cases} \tag{8}$$

3) Permutation Tests: Fisher introduced the permutation test in 1936 [26].

Assuming you want to distinguish between two groups based on height measurements, one can calculate a relevant quantity, such as the difference in average heights. By comparing this value to those obtained from randomly extracting two new groups with the same cardinality $\mathcal{N}_p$ times, it becomes possible to determine whether the original groups are different or equal. If the two groups are homogeneous, the measurements will yield similar results, while they will differ significantly each time if the groups are heterogeneous.

Mathematically, when presented with two statistical populations, A and B, of any size, it becomes feasible to conduct a significance test to assess a specific hypothesis, $\mathcal{H}_0$ or $\mathcal{H}_1$. This involves appropriately defining a test statistic, $T(X)$, and estimating the $p - value\,(\hat{p})$. The estimation process involves iterative performing the measurement $T(X)$, $\mathcal{N}_p$ times over new populations, denoted as $\tilde{A}$ and $\tilde{B}$, which have the same cardinalities as the original ones. These populations are randomly drawn from the pooled ensemble. The resulting $\hat{p}$ is determined by counting how many times the measurements T^* over the permuted populations exceed the value of $T(X)$ over the original population (T_0) [27] [28]. In formulas

$$\hat{p} = \frac{\#(T^* > T_0)}{\mathcal{N}_p}. \tag{9}$$

The *caveat* on the accepted transformations of the data is that they must be likelihood-invariant, meaning they should remain equally likely under the tested hypothesis. In simpler terms, if there is a paired dependence between the units of the populations, the transformation must preserve this dependence to ensure the condition is maintained, thereby making the test exact.

Finally, the significance test demonstrates H_0 with a significance level α if $\hat{p} < \alpha$, where α can be fixed equal to a certain value or *adaptively* updated like it will be shown later on (Section III). It's noteworthy that $\hat{p}$ asymptotically approaches the true one, indicating that with a higher number of permutations $\mathcal{N}_p$, the bias in the estimation decreases. Importantly, not all possible permutations are required for a reliable estimation; the optimal number depends on the specific application and the characteristics of the test statistic. In designing such operations, a common strategy involves defining a test that leverages known or expected properties of the distributions being analyzed (e.g., expected probability distribution functions, known symmetry properties). This ensures that the test statistic is stochastically greater under H_1 than under H_0. Further details can be found in [27] [28].

III. CHANGE POINT DETECTION (CPD)

Before starting the detection on the i_{th} line of $\hat{\Gamma}$, a preliminary check is performed considering a noise threshold th_n.

The threshold is determined by modeling the probability distribution of N_r independent realizations of the maximum of the noise coherence matrix, by the *Generalized Extreme Value distribution* theory [29]. Taking $\gamma_n \in [0,1]^W$, the vector containing W equispaced values between 0 and 1, and fixing the number of looks L, it is possible to approximate the probability density function of a single realization r of the maximum of the noise coherence matrix as

$$\begin{cases} f_j(\gamma_n; L) = k\sqrt{L}\left(\sqrt{L}\gamma_n\right)^{k-1} e^{-\left(\sqrt{L}\gamma_n\right)^k}, \\ k = \left|2 - e^{-L+5}\right|, \end{cases} \quad (10)$$

for large L ($L > 5$). The approximation is obtained through Monte Carlo simulations by generating estimates of the maximum of the theoretical noise coherence matrix, varying L.

Considering now the N_r independent realizations, the joint probability density function will be

$$f(\gamma_n; L) = \prod_{r=1}^{N_r} f_r(\gamma_n; L), \quad (11)$$

and by setting a value of tolerance p_e, th_n is the value satisfying

$$p_e = \int_0^{th_n} f(\gamma_n; L)\, d\gamma_n. \quad (12)$$

Observing the dual function performed by th_n is noteworthy. Specifically, it not only speeds up the detection step when dealing with noisy lines in $\hat{\Gamma}$, but also helps to accurately identify a potential single blocks structure within it, regardless of its position.

A. Screening and Candidates Selection

For each line represented by $\hat{\gamma}_i \in [0,1]^{NI}$ in $\hat{\Gamma}$, the algorithms calculates a screening function s for the selection of the candidate change points (C-CPs) if $\max(\hat{\gamma}_i) > th_n$. The rationale behind s design is straightforward: in the presence of a change point (CP), $\hat{\gamma}_i$ resembles a vector with consecutive samples showing a sudden variance change at the CP sample. In an ideal scenario without noise, the CP can be directly identified by progressively separating the vector into two populations and comparing their maxima. In formulas, $s \in [0,1]^{(NI-i)-1}$ is defined as

$$s(j - i) = \max_{k=i+1,...,j} \hat{\gamma}_i(k) \; - \max_{h=j+1,...,NI} \hat{\gamma}_i(h), \quad (13)$$

$$\forall j = i+1, i+2, ..., NI - 1.$$

However, in a realistic scenario where $\hat{\gamma}_i$ is affected by noise, solely relying on s is insufficient. Even though valuable properties of the function near the candidate change points can still be recovered. Candidate changes are recognized as local maxima and flex points of s. Considering $\hat{\gamma}_i$ and defining $\mathcal{Z} \subseteq \mathcal{D}$ as $\mathcal{Z} = \{i+1, ..., NI-1\}$

$$\text{C-CPs} = \{z \in \mathcal{Z} \,\big|\, \Delta s(z) = 0, \, \Delta^2 s(z) = 0\}. \quad (14)$$

If $\#\text{C-CPs} \neq 0$, the CPD continues; otherwise it repeats the same operations on the next line. This situation is common for targets that are either not coherent from the beginning or are undergoing changes without directly leading to adjacent blocks (e.g., material that is compacting).

B. Candidate Election

It elects the C-CP among the C-CPs. The election is carried out through unpaired permutation tests. The preference for this type of test over classical statistical hypothesis tests is driven by its nonparametric nature and its flexibility in customizing a test statistic based on the application, which maximizes the utilization of information inherent in the data. Moreover, the classical integral calculus for the computation of the $p-value$ is now replaced by a Monte Carlo simulation.

Given the C-CPs at $\hat{\gamma}_i$, if a real abrupt change happens at index $z^* \in$ C-CPs then

$$\hat{\gamma}_{i+z^*}^{(nr)} = \hat{\gamma}^{(nr)} = \begin{bmatrix} \hat{\gamma}_{i+z^*}(i) \\ \hat{\gamma}_{i+z^*}(i+1) \\ \vdots \\ \hat{\gamma}_{i+z^*}(i+z^*-1) \end{bmatrix} \quad (15)$$

$$\sim Rayleigh\left(\sqrt{\frac{1}{2L}}\right),$$

meaning that the observed samples before z^* at the $(i+z^*)_{th}$ line, namely the *noise restricted*, is identically distributed like noise ($\mathcal{H}_0$). This assumption is the basis for the choice of the test statistic $T(X)$: what it must compare is the empirical distribution function of $\hat{\gamma}^{(nr)}$, $\mathcal{F}_{\hat{\gamma}^{(nr)}}(X)$, with the theoretical $\mathcal{F}_{th}(X) \sim Rayleigh\left(\sqrt{\frac{1}{2L}}\right)$. One good example of $T(X)$ is the two-sided *Kolmogorov-Smirnov statistic*, in formulas

$$T(X) = \sup_X \left|\mathcal{F}_{\hat{\gamma}^{(nr)}}(X) - \mathcal{F}_{th}(X)\right|. \quad (16)$$

The last point to address is how to set a reliable $\mathcal{N}_p$. The criterion followed is based on the sensitivity with which CPD must work, i.e., how accurate must be $\hat{p}$ for the given $\hat{\gamma}^{(nr)}$. A wise choice is to privilege the cases when $\#\hat{\gamma}^{(nr)}$ is low, i.e., short-term changes because they are much more difficult to detect and a good estimation of $p-value$ makes the step much more robust. In the opposite cases, lower $\mathcal{N}_p$ can be accepted because of the effectiveness of the designed test statistic and because of the other PCD's steps which play a fundamental role in the case of very long-term changes, where the temporal decorrelation can determine false alarms or missing detections. Moreover, it is worth noticing that the estimation of p by permutation tests in this particular working context is much more affected by L than $\mathcal{N}_p$. By this reasoning, the decision to rule $\mathcal{N}_p$ as follows

$$\mathcal{N}_p = \begin{cases} 20 + \left\lceil \frac{NI}{2} \right\rceil & \text{if } \binom{2\#\hat{\gamma}^{(nr)}}{\#\hat{\gamma}^{(nr)}} > 10^3, \\ \binom{2\#\hat{\gamma}^{(nr)}}{\#\hat{\gamma}^{(nr)}} & \text{otherwise.} \end{cases} \quad (17)$$

where the condition $\binom{2\#\hat{\gamma}^{(nr)}}{\#\hat{\gamma}^{(nr)}} > 10^3$ is setting the threshold on the maximum cardinality for which the estimation of $\hat{p}$ will be exact, privileging the cases where $\#\hat{\gamma}^{(nr)} \leq 6$. After the estimation of all the $\hat{p} - values$, are kept only the points demonstrating $\mathcal{H}_0$, meaning that the eligible C-CPs (C-CPs$_e$) are

$$\text{C-CPs}_e = \left\{ z \in \text{C-CPs} \,\middle|\, \hat{p}(z) < \alpha = (\#\text{C-CPs} + 1)^{-2} \right\}. \quad (18)$$

The significance level α is adaptive due to the influence of noise on the calculation of the C-CPs (14). As L decreases, the noise's impact on the coherence matrix estimation increases, leading to a larger number of elements in C-CP. By introducing a dependence of α on the cardinality of C-CPs, more stringent conditions are imposed for demonstrating $\mathcal{H}_0$. In other words, even with a substantial impact of noise, the probability of rejecting $\mathcal{H}_0$ when it is true becomes very low.

Finally, the C-CP is the point among the C-CPs$_e$ having the maximum $\hat{p}$.

C. Cross-Validation

It cross-validates or re-elects the C-CP. It serves a dual purpose. In the case of short-term changes, it re-validates the CP. Simultaneously, it prevents the misclassification of CP by verifying whether it is attributed to decorrelation phenomena. The approach is similar to the initial election, but now the PCD employs a classical Kolmogorov-Smirnov (KS) test. Starting from the line corresponding to the change and moving along the diagonal, the cross-validation confirms genuine changes identified by permutation tests. If the change is not real, it continues until encountering $\mathcal{H}_0$, updating the CP accordingly.

IV. CHANGE POINT VALIDATION (CPV)

CPV aims to validate the C-CP found in the detection step. Given $\hat{\gamma}_i$ and the relative C-CP, the CPD isolates a priori the candidate noise block $\mathcal{N}$ (6) and tests if it is distributed like
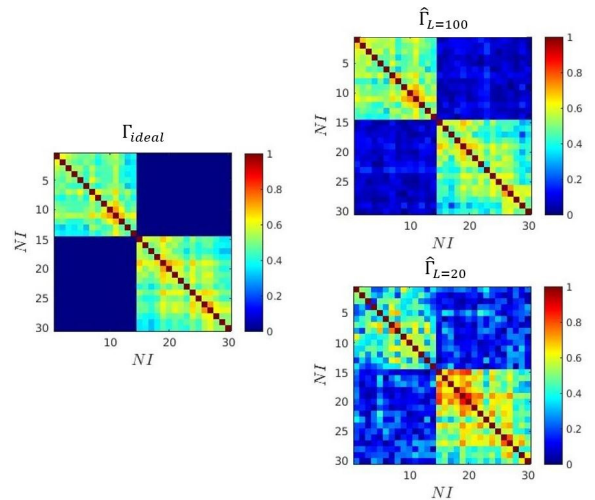

Fig. 5. On the left the model Γ_{ideal}, on the right two different estimations by using a number of looks $L = 100$ and $L = 20$, respectively on the top and the bottom. The lower L, the higher the impact of the outliers at highest B_t.

noise. The effectiveness of the validation step is attributed to the availability of double information about the initiation and conclusion of the block. This enables a transition from a one-dimensional space, delineated by the line, to a two-dimensional space. Within this expanded space, the PCD comprehensively evaluates coherence across all images in $\mathcal{N}$.

A. Noise Block Validation

After the extraction of $\mathcal{N}$, the validation is carried out through a two-sided *Anderson-Darling test* where the probability distribution of $\mathcal{N}$ is tested against the theoretical one, to demonstrate $\mathcal{H}_0$. This choice is due to the statistical power of the Anderson-Darling compared with other similar approaches, as deeply addressed in [30] [31]. Moreover, the direct comparison between $\mathcal{N}$ and a statistical population fitting the theoretical noise distribution implies that the algorithm is not dependent on the size ratio that can eventually characterize $\mathcal{B}$ and $\mathcal{N}$. Because of the complexity and robustness of CPD, it is possible to relax the condition on the significance level α, putting it equal to 0.05.

B. Cross-Validation

The same CPD's cross-check is performed again to prevent misclassifications due to the possible presence of outliers in $\mathcal{N}$ due to the estimation noise.

As it is possible to note in Figure 5 estimating the same ideal coherence matrix by using $L = 100$ and $L = 20$, the estimation noise translates into outliers at highest B_t which will affect the tails of the distribution.

V. PCD OUTPUTS

The PCD produces two different outputs:

- *Change Detection Matrix* (CDM): a matrix of the same dimension of $\hat{\Gamma}$, showing the estimated block model
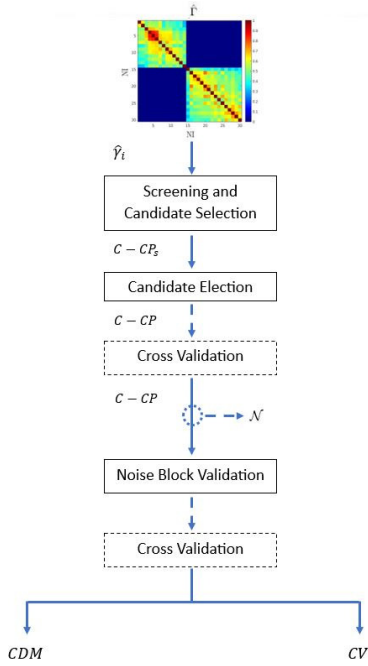
Fig. 6. PCD block scheme.

fitting the coherence matrix. It is filled following these rules:

- Every time the condition on th_n is not met or no C-CPs have been found during CPD, the correspondent line and column are filled with 0.5;
- Every time a CP is found, the PCD fills the correspondent block $\mathcal{B}$ in the CDM with 1 or 2, respectively if the C-CP has not or has been re-elected during the cross-validation;

- *Change Vectors* (CV): the CV is simply a vector of length equal to NI where the entries are one if a change happens at the correspondent image. In particular, the exploitation of the information stored in the CV is useful to design and create different outputs dependent on the particular application.

The final PCD block scheme is shown in Figure 6.

VI. PERFORMANCE ANALYSIS

This section provides a detailed description of the performance of the PCD varying the number of looks L and NI, assuming that the extension of the blocks is $\left\lceil \frac{NI}{\#\mathcal{B}} \right\rceil$, and accepting a detection error of two temporal samples.

A. Metrics

The problem solved by the PCD can be reformulated as a classification task. In this task, the algorithm must analyze the temporal evolution of each pixel and identify noteworthy changes. The assessment involves defining true and false positives, as well as true and false negatives, characterized as follows:

$\frac{\tau}{t_r}$	$\frac{B_n}{B_c}$	L	$\#\mathcal{B}$	NI
30	[-0.15, 0.15]	5,..,25	2,3	30, ..., 60

- True Positive (TP): is an outcome where the PCD correctly predicts the *change* class;
- True Negative (TN): is an outcome where the PCD correctly predicts the *no-change* class;
- False Positive (FP): is an outcome where the PCD predicts the *change* class instead of the *no-change* class;
- False Negative (FN): is an outcome where the PCD predicts the *no-change* class instead of the *change* class.

These quantities are subsequently utilized to compute the following metrics:

- *Accuracy* (ACC): It is the overall correctness

$$\text{ACC} = \frac{\text{TP+TN}}{\text{TN+FP+TP+FN}}; \qquad (19)$$

- *F1 score* (F1): It measures the algorithm's reliability

$$\text{F1} = \frac{2 * \text{PRE} * \text{REC}}{\text{PRE+REC}}, \qquad (20)$$

where

- *Precision* (PRE): It is the capability of predicting the positive category

$$\text{PRE} = \frac{\text{TP}}{\text{TP+FP}}; \qquad (21)$$

- *Recall* (REC): It is the ability to detect the positive category

$$\text{REC} = \frac{\text{TP}}{\text{TP+FN}}. \qquad (22)$$

B. Simulation settings and results

The performance has been measured out of 5000 Monte Carlo simulations in the cases where $\#\mathcal{B} = 2, 3$ with same cardinality, assuming NI regular acquisitions with satellite revisit time t_r equal to 12 days, $B_n \in \mathcal{U}([-200, 200])$ [m] and B_c equal to 1300. The number of looks and images varies respectively as $L = 5, ..., 25$ and $NI = 30, ..., 60$ (Table I). Figure 7 shows on the left the F1 and on the right the ACC estimates out of the simulations as a function of L and NI when $\#\mathcal{B} = 2, 3$, respectively on the top and the bottom. The metrics demonstrate improvement as the number of looks L increases. This enhancement can be attributed to the more accurate estimation of $\hat{\Gamma}$. Specifically, there is an increase from 0.57 to 0.74 in F1 when $\#\mathcal{B} = 2$, and a rise from 0.70 to 0.82 in other cases while maintaining a consistently high level of overall accuracy. The performance is observed to be correlated with both the number of change points and the length of the dataset. Specifically, a higher number of CPs corresponds to better performance, especially at higher values of NI. This relationship is depicted in a plane characterized by the parameters L and NI, as illustrated in Figure 7. Figure 8 provides evidence supporting the aforementioned considerations. By modifying the parameters outlined in Table
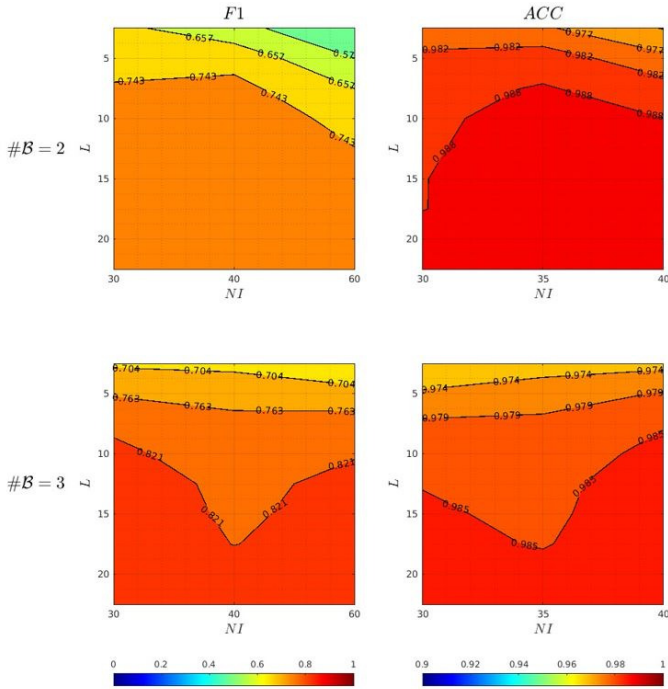
Fig. 7. PCD's F1 score on the left and ACC on the right, in the case of two and three blocks of equal extension, respectively, on the top and the bottom. The results are shown as a function of the number of images NI and of the number of looks L. The performances improve by increasing the number of looks L as well as the higher the number of CPs, the better the performance with a longer dataset.

Fig. 8. On the left F1 and the right ACC, in dependence on the number of looks L and the number of images NI, by putting the number of blocks $\#\mathcal{B}$ equal to 2 and 4 respectively on the top and the bottom. The knee of the curves moves along NI, by increasing $\#\mathcal{B}$.

Fig. 9. PCD's F1 as a function of the cardinality of the block, in the case $NI = 30$ and $L = 10, 20, 30$. The performance starts to be acceptable, namely F1 ≥ 0.6, when $5 < \text{card}(\mathcal{B}) \leq 7$. This represents the lower bound on the minimum detectable change.

I, setting $L = 10, 20, 40$ and $\#\mathcal{B} = 2, 4$, and evaluating F1 and ACC by 5000 Monte Carlo simulations, the shapes of the functions change following the considered parameters: it decreases by lowering L and moves the location of the knee by increasing $\#\mathcal{B}$. An important observation pertains to the behavior of F1 in the case of low $\#\mathcal{B}$ and high NI. Performance tends to decline due to the impact of temporal decorrelation. It is challenging to recognize blocks structure when their extension exceeds τ.

The performance is also dependent on the block cardinality. For this reason, an analysis has been conducted in the case of $NI = 30$ and $L = 10, 20, 30$, and modeling the quantities related to the geometry as in Table I. In particular, the performance in terms of F1 has been calculated for a block cardinality $\text{card}(\mathcal{B}) = 3, ..., 12$. As it is possible to note in Figure 9, the performance of the PCD is acceptable (F1 ≥ 0.6), from a cardinality $5 < \text{card}(\mathcal{B}) \leq 7$. This result provides evidence of the minimum sensitivity of the algorithm. Based on the earlier discussions, it can be concluded that this lower limit remains applicable even when dealing with a larger dataset.

So far, the performance has been measured in the case of two or more adjacent blocks inside the coherence matrix. It can also happen that the observed target is coherent only for a restricted portion of the observation time, translating into a single block's presence. In dependence on its temporal location, it is possible to define:

- DCS (Disappearing Coherent Scatterer): the target is coherent only in the first part of the observation time;
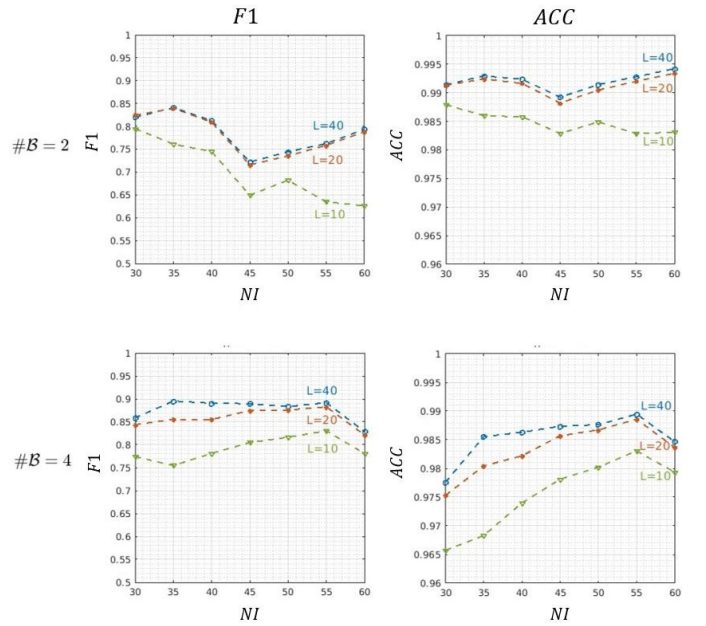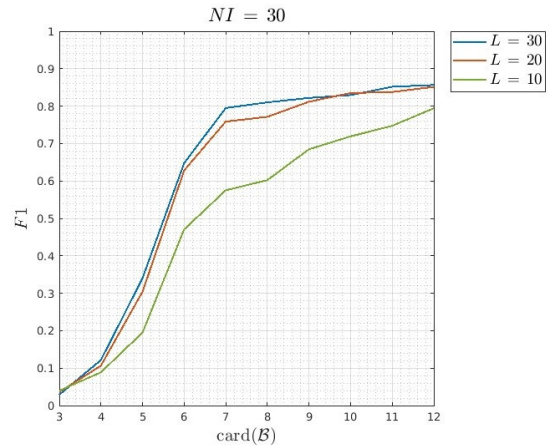
- ACS (Appearing Coherent Scatterer): the target is coherent only in the last part of the observation time;
- ADCS (Appearing Disappearing Coherent Scatterer): the target is coherent only for a generic portion of the observation time.

The presence of such kinds of targets is generally related to rapidly changing environments and in particular, to non-stationary noise sources affecting the radar return from the ground, i.e., clutter noise. To address this final analysis, the performance of the PCD has been measured for the ADCS case, being the most generic and challenging one. Moreover, the non-stationary noise sources have been modeled by simply corrupting a certain amount of pixels within the block. The
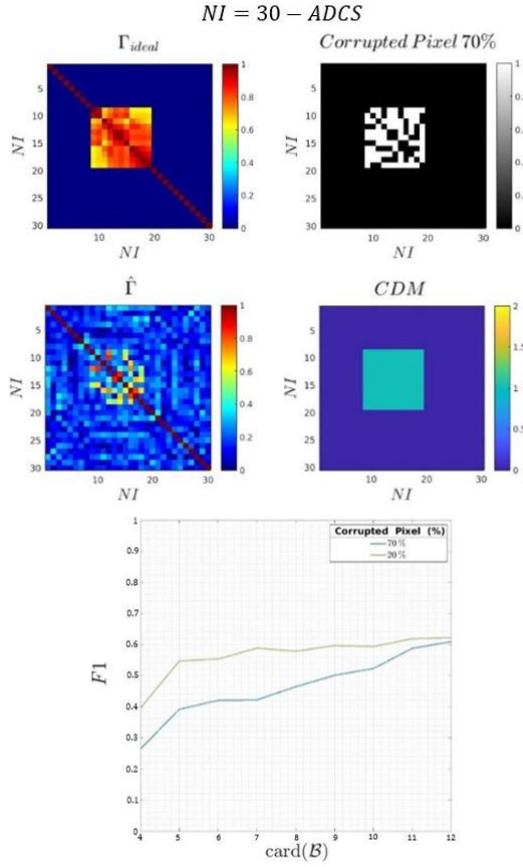
Fig. 10. PCD's F1 in case of an Appearing Disappearing Coherent Scatterer (ADCS) as a function of the cardinality of the block, assuming the 20 % and 70 % of corrupted pixels within the block, in the case $NI = 30$ and $L = 20$. On the top an example in the case of the 70 % of corrupted pixels. From left to right are respectively the ideal ADCS model, the map of corrupted pixels, the estimation of the coherence matrix and the relative CDM. On the bottom, the performance in terms of F1.

corrupted pixels are the ones below a threshold calculated from the pth percentile of γ_b (2) within the block, where p^{th} indicates the percentage of pixels to be corrupted. Finally, the performance has been measured by varying the cardinality of the block, in the case of $NI = 30$ and number of looks $L = 20$. Figure 10 presents the simulation results. As it is possible to note, these results not only confirm what has already been discussed about the dependence on card($\mathcal{B}$) but add useful insights about the robustness of the proposed methods to cope with very challenging cases. In particular, in the 20 % case the PCD shows good detection capability for card($\mathcal{B}$) ≥ 7. In the other case, although the huge amount of corrupted pixels, the PCD is still able to spot the target if card($\mathcal{B}$) > 10.

In conclusion, PCD shows robustness and very high sensitivity in detecting abrupt coherence changes without making assumptions about their number. The performance is dependent both on L because of the quality of the estimation of the coherence matrix, but also on NI and consequently on $\#\mathcal{B}$ and card($\mathcal{B}$). In particular, it has been shown that in the case $\#\mathcal{B} > 1$, the PCD reaches F1 ≥ 0.6 for L ≥ 5, for a minimum cardinality ranging in card($\mathcal{B}$) ≥ 7. Assuming instead the

case $\#\mathcal{B} = 1$, generally not only due to a very dynamic environment but also to non-stationary noise sources, the PCD still exhibits the same F1 and minimum detectable cardinality performance if the percentage of the corrupted pixels within the block is at maximum the 20 %. The higher the percentage, the higher the minimum detectable cardinality (the 70 % requires as minimum card($\mathcal{B}$) = 10).

VII. COMPARISON WITH EXISTING METHODS

The insights and comments derived regarding the PCD are highly valuable and are a crucial foundation for comprehending the forthcoming comparison with other algorithms. This comparative analysis will include the GLRT-CCD algorithm presented in [10] [11], the Omnibus detector described in [14] and [15], and the REACTIV [16].

The initial approach relies on the Generalized Likelihood Ratio Test (GLRT). This method involves comparing the posterior probabilities of the observations under the null hypothesis $\mathcal{H}_0$, assuming no changes have occurred, with the alternative hypothesis $\mathcal{H}_1$, which posits a change after e certain amount of acquisitions. Calling as y the vector of the NI acquisitions, and as f the posterior probability density functions, the Likelihood Ratio (LR) for point targets is

$$\Lambda_{PS}(y) = \frac{f(y|\mathcal{H}_0)}{f(y|\mathcal{H}_1)} \tag{23}$$

where the modeling of the pdf is deeply addressed in [10]. Instead, in the case of distributed scatterers, the LR can be stated as

$$\Lambda_{DS}(L, \mathbf{Y}) = L \left(\log \left(\frac{|\Gamma_1|}{|\Gamma_0|} \right) + \gamma_{WY} \right) ,$$
$$\mathbf{W} = \Gamma_1^{-1} - \Gamma_0^{-1} , \tag{24}$$
$$\gamma_{WY} = Tr \left(\mathbf{W}\hat{\Gamma}_Y \right) ,$$

where $\mathbf{W}$ is the matrix of the weights, $\mathbf{Y}$ is the matrix containing all the L looks, and $\Gamma_{0,1}$ the theoretical coherence matrix models respectively under $\mathcal{H}_{0,1}$. Intuitively, the LR serves as a measure of how closely $\hat{\Gamma}_Y$ resembles a coherence matrix exhibiting a blocks structure (7). The identification of single or multiple change points is facilitated by leveraging a distinctive property of the LR functions described by equations (23) and (24). These functions exhibit a pronounced deep minimum in the case of a single change or multiple local minima in the presence of multiple changes. From the last consideration, it follows that

$$\text{CPs}_{PS} = \{i \in \mathcal{D} \,|\, \min \left(\Lambda_{PS}(y) \right) < \mathcal{T}\}, \tag{25}$$

and

$$\text{CPs}_{DS} = \{i \in \mathcal{D} \,|\, \min \left(\Lambda_{DS}(L, \mathbf{Y}) \right) < \mathcal{T}\}, \tag{26}$$

where $\mathcal{T}$ is the threshold under which $\mathcal{H}_0$ is rejected, whose choice is crucial. In the case of multiple changes, the algorithm is applied recursively over the identified blocks at the previous iteration [10] [11].

To facilitate a comparison between the PCD and the GLRT-CCD, an adaptive threshold evaluation has been implemented, inspired by the same rationale as in (12). Utilizing the indices
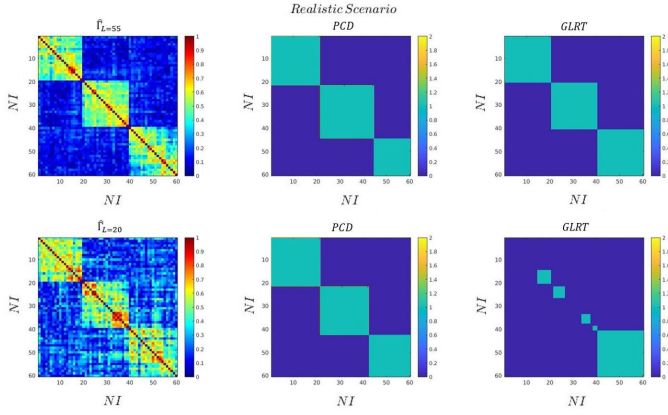
Fig. 11. Example of CDM out of the PCD and the GLRT-CCD methods, in a realistic scenario (Table I) considering sixty images, three blocks of equal extension, and a number of looks equal to fifty-five and twenty, respectively on the first and the second row. As it is possible to note, PCD is robust even with a few number of looks. Conversely, GLRT-CCD can be jammed by the impact of baseline decorrelation.

TABLE II
SIMULATION PARAMETERS: IDEAL SCENARIO.

$\frac{\tau}{t_r}$	$\frac{B_n}{B_c}$	L	$\#\mathcal{B}$	NI
20	[-0.007, 0.007]	20, ..., 55	2	40

TABLE III
SIMULATION PARAMETERS: REALISTIC SCENARIO.

$\frac{\tau}{t_r}$	$\frac{B_n}{B_c}$	L	$\#\mathcal{B}$	NI
10	[-0.15, 0.15]	20, .., 55	2	40

- Ideal Scenario: with a negligible amount of geometrical and temporal decorrelation. The simulation parameters are in Table II;
- Realistic Scenario: with geometrical and temporal decorrelation. The simulation parameters are in Table III.

The evaluation is based on the F1 score for all algorithms, measured through 5000 Monte Carlo simulations in the specified scenarios. Subsequently, the F1 score for PCD is individually combined with the F1 scores of the other considered algorithms to form a new metric named F1 Ratio, or $F1R$, defined as

$$F1R = \frac{F1_{PCD}}{F1_*}, \qquad (28)$$

where the symbol $*$ indicates any of the other algorithms.

The results of the simulations are shown in Figure 12, where $F1R$ is expressed in dB. The GLRT-CCD, as expected, performs better in the ideal scenario, with a gain increasing with L. Instead, in a more realistic scenario, PCD exhibits greater robustness, particularly at lower L, where it achieves significantly higher $F1R$ values. Notably, the GLRT approach begins to perform comparably to the PCD at a very high number of looks. This is attributed to the improved quality in the estimation of the coherence matrix and a more relaxed temporal decorrelation coefficient τ.

The PCD always performs better than the REACTIV in both scenarios and the Omnibus only in the realistic scenario. In the ideal scenario, the PCD demonstrates better performance than the Omnibus only at higher numbers of looks, with comparable performance as the number of looks decreases. It's

of the minima of the LR function (23) (24), the detected change points can be validated by comparing the maximum value in $\mathcal{N}$ with th_n. In this way, calling as C-CPs the minima of the LR function (23) (24), and as $\mathcal{N}_{CCP}$ the noise block associated to a given C-CP, then (25) and (26) can be rephrased as

$$\text{CPs} = \{i \in \mathcal{D} \mid \max\left(\mathcal{N}_{CCP}\right) < th_n\}. \qquad (27)$$

In the initial comparison between the two approaches, the analysis of the CDM is conducted using the parameter settings outlined in Table I. This evaluation considers $NI = 60$, $\#\mathcal{B} = 3$ with equal extension, and $\hat{\Gamma}$ estimated through $L = 55, 20$. In a realistic scenario, the impact of both estimation noise and decorrelation mechanisms on the coherence matrix significantly affects the model estimated through GLRT-CCD (Figure 11). Specifically, the two approaches yield identical results when $L = 55$. However, when $L = 20$, only the PCD estimate is preserved. Instead, the GLRT-CCD estimate is jeopardized by the presence of both baseline and temporal correlation, which are indeed moderate, but not considered in the model (24), resulting in the fragmentation of the estimated CDM in many small blocks.

Moving on to the other algorithms, the Omnibus detector [14] [15] examines whether the polarimetric covariance matrices in a SAR dataset of NI images are all equal (H0) or not ($\mathcal{H}_1$) through a Likelihood Ratio Test detailed in [15]. In contrast, the REACTIV detector encodes the temporal coefficient of variation [3], as the saturation in the HSV color space. The outcome is a binary map where saturated pixels indicate changes. As both algorithms emphasize changed pixels in a SAR image, they have been adapted to enable a fair comparison. Both algorithms are applied to successive pairs of images, highlighting temporal changes based on the principles outlined in [14] [16].

To conduct a quantitative comparison between the algorithms, the assessment is carried out by considering blocks of equal extension in two distinct scenarios:
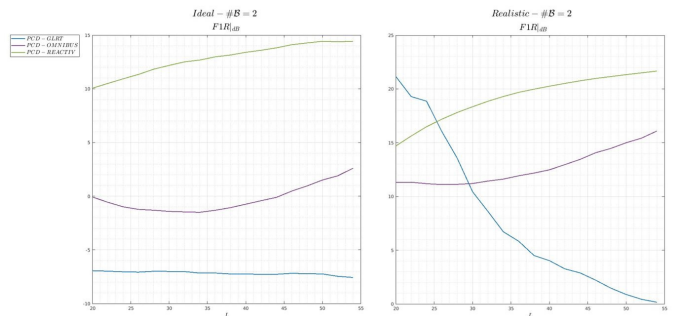

Fig. 12. $F1R$ [dB] in the case of the ideal and realistic scenario, respectively on the left and the right, considering two blocks of equal extension and a number of images $NI = 40$.
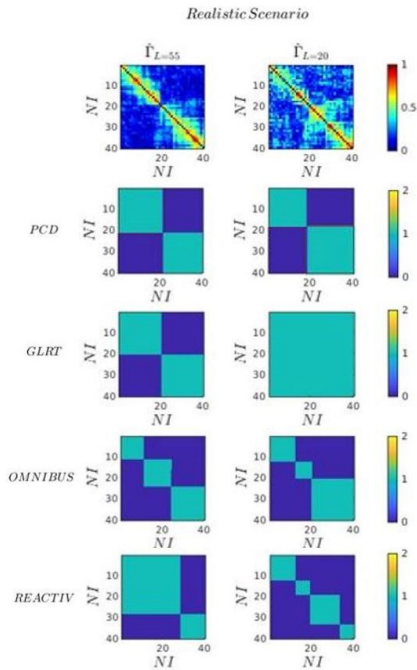
Fig. 13. Examples of CDM of all the compared algorithms in the case of realistic scenario, for a number of looks equal to 55 and 20, respectively, on the left and the right. PCD can spot the changes even in strong noise and in case of not negligible temporal decorrelation impact; instead, the GLRT tends to recognize blocks structure even with not negligible temporal decorrelation, only in case of a high number of looks. Omnibus and REACTIV tend to consider as CP also subtle changes in coherence that can be due to simple estimation noise.
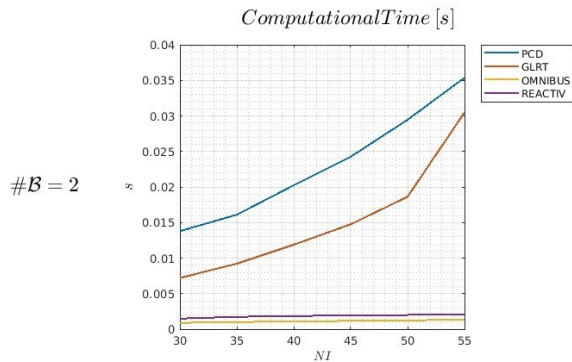

Fig. 14. Comparison of the computational times as a function of the number of images NI, in the case of two and three blocks.

important to note that the performances of both detectors may be underestimated as they are adapted for a specific purpose. Figure 13 shows examples of CDM from all the compared algorithms in the realistic scenario case. The number of looks is fixed at $L = 55, 20,$ respectively, on the left and the right. In both cases, the PCD is capable of detecting changes even in the presence of strong noise and higher temporal decorrelation impact; instead, the GLRT tends to recognize blocks structure even with not negligible temporal decorrelation, only in case of a high number of looks. Concerning the Omnibus, even if it has been adapted for this particular purpose, it is correctly spotting the CP in both cases, but it tends to consider as CP

TABLE IV
SIMULATION PARAMETERS: COMPUTATIONAL TIME.

$\frac{\tau}{t_r}$	$\frac{B_n}{B_c}$	L	$\#\mathcal{B}$	NI
30	[-0.15, 0.15]	55	2	30, ..., 55

also subtle changes in coherence that can be due to simple estimation noise. The same happens for the REACTIV, leading to the conclusion that PCD exhibits greater accuracy in these scenarios.

In conclusion, all the tested algorithms are compared in terms of computational time by varying the dataset length, ranging from $NI = 30, ..., 55$. The comparison is done by arbitrarily fixing $L = 55$ because the computational time is independent of the number of looks. The simulation settings are summarized in Table IV. As expected, the Omnibus and the REACTIV approaches are faster, gaining, on average, one order of magnitude concerning the PCD and the GLRT-CCD algorithms (Figure 14). Additionally, it's noteworthy that the computational time for the PCD and GLRT-CCD algorithms is influenced by the length of the dataset and the number of CPs, unlike the Omnibus and REACTIV. In conclusion, while the PCD provides superior overall performance compared to the other algorithms, it comes with a non-negligible computational effort.

VIII. AUGUST 2016, CENTRAL ITALY EARTHQUAKE

The validation of the algorithm is performed through the analysis of data acquired in 2016 over Amatrice, central Italy. The choice is due to the seismic events that happened on 24 August 2016, with the epicenter in the comune of Accumoli, at the north of the processed area: this was the largest tremor since 2009 when another earthquake event happened in the Abruzzo region. This event was followed by several other aftershocks, 2500 estimated, until the end of August. Three of the strongest happened in Amatrice between 24 and 26 August 2016, destroying half of the town. The processed datasets are two Sentinel-I stacks of ascending and descending S1A and S1B passes, both of them with VV polarization. The descending dataset, track 22, is composed of 15 images from 18 March 2016 to 14 September 2016; the ascending dataset, track 117, is composed of 16 images from 24 March 2016 to 26 September 2016. Due to the presence of rural areas where the decorrelation phenomena can strongly impact the final results, the method proposed in [32] has been used to provide an optimum phase filtering aimed to maximize the reliability of the analysis. The first result of the analysis is depicted in Figure 15 where the number of changes is represented as a function of temporal epochs. The epochs correspond to groups of two consecutive images. This choice is driven by the detection error tolerance discussed in Section VI. For each dataset, the first acquisitions have been grouped in a single epoch because the number of occurred changes is null. Furthermore, in this way, the sixth epoch corresponds to seismic events in both cases exactly. For the sake of clarity, the table detailing the epochs is also present in Figure 15. As it is

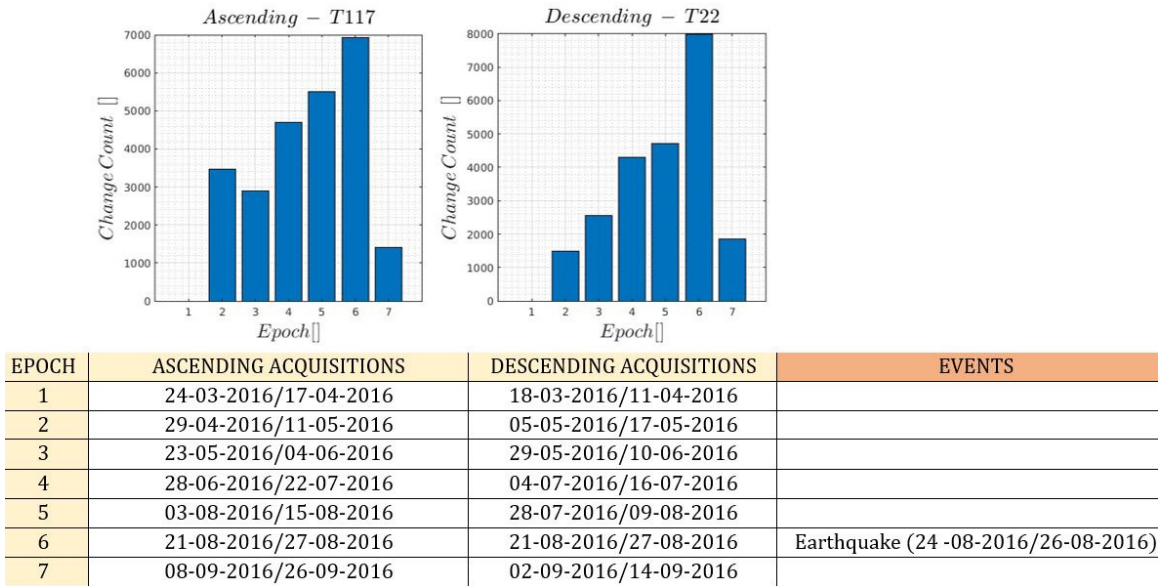| EPOCH	ASCENDING ACQUISITIONS	DESCENDING ACQUISITIONS	EVENTS
1	24-03-2016/17-04-2016	18-03-2016/11-04-2016	
2	29-04-2016/11-05-2016	05-05-2016/17-05-2016	
3	23-05-2016/04-06-2016	29-05-2016/10-06-2016	
4	28-06-2016/22-07-2016	04-07-2016/16-07-2016	
5	03-08-2016/15-08-2016	28-07-2016/09-08-2016	
6	21-08-2016/27-08-2016	21-08-2016/27-08-2016	Earthquake (24 -08-2016/26-08-2016)
7	08-09-2016/26-09-2016	02-09-2016/14-09-2016	

Fig. 15. Central Italy earthquake, number of changes detected by the PCD per acquisition geometry and epoch. In both cases, the peak of the changes corresponds to the seismic event (Epoch 6). Moreover, the number of detected changes in correspondence with the peak is comparable, furnishing a pre-validation of the algorithm.

possible to note, the peak of changes corresponds exactly to the epoch including the seismic events, with comparable values. This aspect is absolutely not negligible because it validates the approach by simply means of the information that can be extracted from the availability of the double geometry over the same areas. An additional aspect regards the shape of the bar plots from the third epoch (May - June 2016): the number of changes, mainly concentrated in the rural areas around the city, is monotonically increasing. This aspect may not be negligible and finds feedback if correlated to the potential pre-earthquake anomalies presented in [33].

After the analysis of the number of detected changes, it is of interest to look inside some of them and visually inspect the blocks structure estimate given by the PCD. Figure 16 shows some examples of CDMs and relative $\hat{\Gamma}$ out of the PCD and the other tested algorithms. The yellow rectangle highlights the total Area of Interest (AOI). Instead, the blue, red and orange squares highlight the portion of AOI from which the examples are taken. The choice was simply driven by the selection of some areas where the estimation of the blocks structure is not so trivial (orange and blue squares) and others where the stability of the radar return guarantees a simpler detection (red square). The blue square presents a typical example of a Temporary Coherent Scatterer (TCS) [5] [6]. As it is possible to note, both the geometries detect the birth of a radar scatterer after the seismic event, with the difference in the coherence time period that is probably due to the different visibility. According to what has been deeply addressed in Section VII, only the PCD and GLRT methods are able to detect the change. Instead, the Omnibus and REACTIV detectors are not tracking the change due to the rapidity of the event. This particular example, in the case of the descending geometry, is also useful to highlight what is stated in Section VI about the minimum cardinality sensitivity of the PCD. In fact, the PCD

correctly detects the first coherence change but it is not able to detect the second one because the cardinality of the block is under its sensitivity. On the other hand, the examples in the orange square highlight the strength of the PCD in coping with more noisy cases. In fact, the ascending case is exactly equal to the example depicted in the blue square, with the difference being that the images forming the block are not constantly correlated with each other. Even if the last group of images is not fully correlated, probably due to the vegetation, there are still not negligible values of coherence that are correctly recognized and detected only by the PCD. The same rationale in a more advanced setting applies for the descending case: even if the majority part of the images composing the first block of the matrix are not correlated, the PCD considers as a block the portion of $\hat{\Gamma}$ described by $\mathcal{I} = \{2, ..., 11\}$, following the notation of equation (4). This happens because of the correlation detected between the second and third images with the eleventh, which is around 0.38 and 0.4. All the other images instead are probably decorrelated not for a change we are interested in, but for physical decorrelation phenomena. Going forward with the comparison between the model estimated by all the approaches, the GLRT in this case is only able to correctly detect the small block at the end of the observation time period in the case of the descending geometry. Instead, the Omnibus and REACTIV detectors are completely missing the detection for the same reasons depicted in the analysis of the blue square case. The examples shown in the red square are taken from an area where the scatterers are predominantly artificial. This aspect guarantees great stability in the radar return, which results in a very low noise estimate of the coherence matrix: in this context, all the approaches for both geometries are performing well. However, the Omnibus detector for the ascending geometry is missing the detection: this is due to the availability of a single polarization channel,
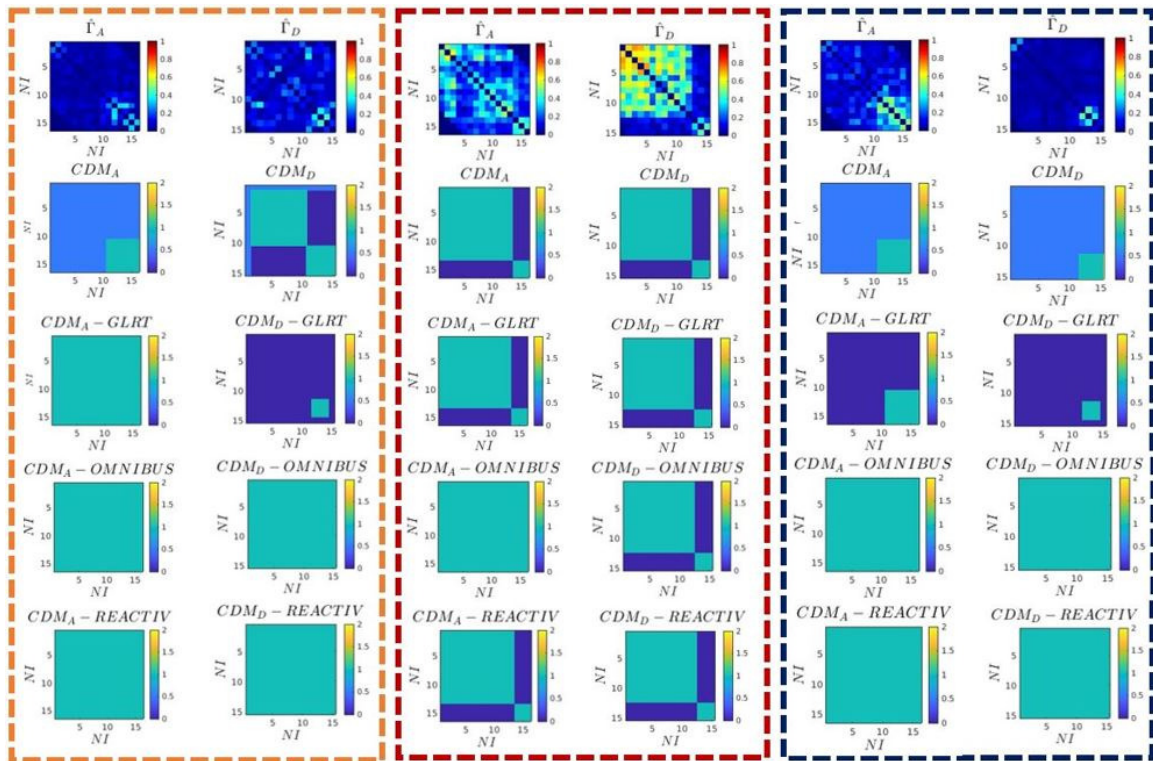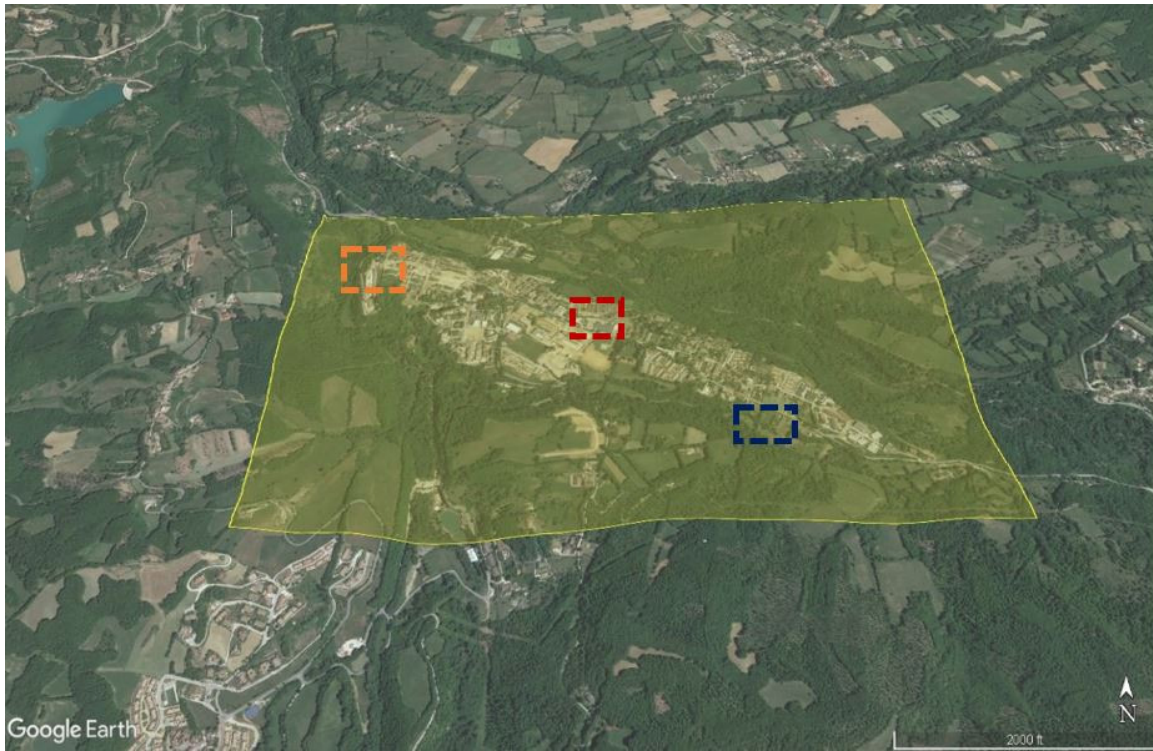
Fig. 16. Examples of CDMs out of PCD, GLRT, Omnibus and REACTIV over Amatrice. The yellow rectangle indicates the Area of Interest. Instead, the orange, red, and blue ones highlight the areas from which the examples have been taken. Notably, the GLRT is able to recognize blocks structure if the value inside the block is constant, but it is also very precise in case of very small block cardinality. The Omnibus and REACTIV detectors are capable of correctly recognizing the changes only in the case of the red rectangle targets, where the low noise estimate of the coherence matrix suggests great stability of the radar return. Notably, even for the red square case, the Omnibus detector is missing the detection of the change for the ascending geometry due to the availability of a single polarization channel. Finally, the PCD can recognize blocks structure even in the presence of very noisy acquisitions but experiences difficulties in case of very small cardinality as analyzed in Figure 9.

which is limiting the detection capabilities of this approach. To conclude, the presented case study validates the method, highlighting the capability of recognizing very challenging block structures and changes even if the impact of both noise and decorrelation is strong. On the contrary, one limitation can be represented by difficulties in coping with very small blocks.

IX. CONCLUSION

This paper presents a nonparametric algorithm for Coherent Change Detection, the Permutational Change Detection, based on the Permutation Tests. This statistical tool allows the users to apply PCD without making strong assumptions about the data and intrinsically guarantees great robustness against stationary and non stationary noise sources. The PCD has been compared with the GLRT-CCD approach and two other change detectors, Omnibus and REACTIV. As shown in Section VII, in the proposed realistic scenario, the PCD seems to perform better, showing great robustness in detecting changes in coherence even in the presence of decorelated pairs, like due to temporal baseline or clutter noise. Instead, considering the absence of decorrelation phenomena, the GLRT approach always performs better than the others. The computational time represents the main limitation, being dependent on NI and how dynamic a target is. It can be reduced using parallelization or strongly reducing the bandwidth of considered images. In this last case, if applied to real data, a deep study of the main atmospheric phenomena as well as of the electromagnetic properties of the area is suggested so that it will be possible to reduce the risk of losing information. Finally in Section VIII the PCD has been applied to real data, and the results are presented in terms of the number of detected changes and examples of them. Thanks to the analyzed examples, is possible to highlight and demonstrate all the features theoretically demonstrated in Section VI and Section VII. Moreover, the joint application of this algorithm during any InSAR analysis can represent a valuable improvement from the point of view of the completeness and exactness of the information recovered from the data. Detecting adjacent changes in the case of fully persistent scatterers and detecting only restricted temporarily coherent windows represent per se information and can enhance the value of the analysis and the reliability of the final results.

REFERENCES

[1] A. Ferretti, C. Prati, and F. Rocca, "Non-uniform motion monitoring using the permanent scatterers technique," *FRINGE'99: Advancing ERS SAR Interferometry from Applications towards Operations*, pp. 1–6, 2000.
[2] ——, "Nonlinear subsidence rate estimation using permanent scatterers in differential SAR interferometry," *IEEE Transactions on geoscience and remote sensing*, vol. 38, no. 5, pp. 2202–2212, 2000.
[3] ——, "Permanent scatterers in SAR interferometry," *IEEE Transactions on geoscience and remote sensing*, vol. 39, no. 1, pp. 8–20, 2001.
[4] A. Ferretti, A. Fumagalli, F. Novali, C. Prati, F. Rocca, and A. Rucci, "A new algorithm for processing interferometric data-stacks: SqueeSAR," *IEEE Transactions on geoscience and remote sensing*, vol. 49, no. 9, pp. 3460–3470, 2011.
[5] F. Hu, J. Wu, L. Chang, and R. F. Hanssen, "Incorporating temporary coherent scatterers in multi-temporal insar using adaptive temporal subsets," *IEEE transactions on geoscience and remote sensing*, vol. 57, no. 10, pp. 7658–7670, 2019.
[6] L. Zhang, X. Ding, and Z. Lu, "Ground settlement monitoring based on temporarily coherent points between two sar acquisitions," *ISPRS Journal of Photogrammetry and Remote Sensing*, vol. 66, no. 1, pp. 146–152, 2011.
[7] E. J. Rignot and J. J. Van Zyl, "Change detection techniques for ERS-1 SAR data," *IEEE Transactions on Geoscience and Remote sensing*, vol. 31, no. 4, pp. 896–906, 1993.
[8] G. Moser and S. B. Serpico, "Generalized minimum-error thresholding for unsupervised change detection from SAR amplitude imagery," *IEEE Transactions on Geoscience and Remote sensing*, vol. 44, no. 10, pp. 2972–2982, 2006.
[9] G. Nico, M. Pappalepore, G. Pasquariello, A. Refice, and S. Samarelli, "Comparison of SAR amplitude vs. coherence flood detection methods-a GIS application," *International Journal of Remote Sensing*, vol. 21, no. 8, pp. 1619–1631, 2000.
[10] A. V. Monti-Guarnieri, M. A. Brovelli, M. Manzoni, M. M. d'Alessandro, M. E. Molinari, and D. Oxoli, "Coherent change detection for multipass SAR," *IEEE Transactions on Geoscience and Remote Sensing*, vol. 56, no. 11, pp. 6811–6822, 2018.
[11] M. Manzoni, A. Monti-Guarnieri, and M. E. Molinari, "Joint exploitation of spaceborne SAR images and gis techniques for urban coherent change detection," *Remote Sensing of Environment*, vol. 253, p. 112152, 2021.
[12] J. Jung, D.-j. Kim, M. Lavalle, and S.-H. Yun, "Coherent change detection using inSAR temporal decorrelation model: A case study for volcanic ash detection," *IEEE Transactions on Geoscience and Remote Sensing*, vol. 54, no. 10, pp. 5765–5775, 2016.
[13] P. Mastro, G. Masiello, C. Serio, and A. Pepe, "Change detection techniques with synthetic aperture radar images: Experiments with random forests and sentinel-1 observations," *Remote Sensing*, vol. 14, no. 14, p. 3323, 2022.
[14] A. A. Nielsen, K. Conradsen, and H. Skriver, "Omnibus test for change detection in a time sequence of polarimetric sar data," in *2016 IEEE International Geoscience and Remote Sensing Symposium (IGARSS)*. IEEE, 2016, pp. 3398–3401.
[15] K. Conradsen, A. A. Nielsen, and H. Skriver, "Determining the points of change in time series of polarimetric sar data," *IEEE Transactions on Geoscience and Remote Sensing*, vol. 54, no. 5, pp. 3007–3024, 2016.
[16] E. Colin Koeniguer and J.-M. Nicolas, "Change detection based on the coefficient of variation in sar time-series of urban areas," *Remote Sensing*, vol. 12, no. 13, p. 2089, 2020.
[17] A. M. Guarnieri and S. Tebaldini, "On the exploitation of target statistics for SAR interferometry applications," *IEEE Transactions on Geoscience and Remote Sensing*, vol. 46, no. 11, pp. 3436–3443, 2008.
[18] A. Monti-Guarnieri, M. Manzoni, D. Giudici, A. Recchia, and S. Tebaldini, "Vegetated target decorrelation in sar and interferometry: models, simulation, and performance evaluation," *Remote Sensing*, vol. 12, no. 16, p. 2545, 2020.
[19] F. Rocca, "Modeling interferogram stacks," *IEEE Transactions on Geoscience and Remote Sensing*, vol. 45, no. 10, pp. 3289–3299, 2007.
[20] A. Ferretti, *Satellite InSAR Data: reservoir monitoring from space (EET 9)*. EAGE Publications, Kosterijland 48, 3981 AJ Bunnik, The Netherlands, 2014.
[21] R. Bamler and P. Hartl, "Synthetic aperture radar interferometry," *Inverse problems*, vol. 14, no. 4, p. R1, 1998.
[22] R. Touzi, A. Lopes, J. Bruniquel, and P. W. Vachon, "Coherence estimation for SAR imagery," *IEEE Transactions on geoscience and remote sensing*, vol. 37, no. 1, pp. 135–149, 1999.
[23] A. Ferretti, A. Monti-Guarnieri, C. Prati, F. Rocca, and D. Massonet, *InSAR principles-guidelines for SAR interferometry processing and interpretation*. ESA Publications ESTEC Postbus 299, 2200 AG Noordwijk, The Netherlands, 2007, vol. 19.
[24] E. E. Kuruoglu and J. Zerubia, "Modeling sar images with a generalization of the rayleigh distribution," *IEEE Transactions on Image Processing*, vol. 13, no. 4, pp. 527–533, 2004.
[25] A. Ferretti, C. Colesanti, D. Perissin, C. Prati, and F. Rocca, "Evaluating the effect of the observation time on the distribution of SAR permanent scatterers," in *Proc. FRINGE*, 2004, pp. 26–1.
[26] R. A. Fisher, "" The coefficient of racial likeness" and the future of craniometry," *The Journal of the Royal Anthropological Institute of Great Britain and Ireland*, vol. 66, pp. 57–63, 1936.
[27] B. Brown, *Permutation Tests for Complex Data: Theory, Applications and Software by F. Pesarin and L. Salmaso*. John Wiley & Sons Inc, Hoboken, New Jersey, 2012.
[28] P. Good, *Permutation tests: a practical guide to resampling methods for testing hypotheses*. Springer Science & Business Media, New York, NY, 2013.

[29] S. Kotz and S. Nadarajah, *Extreme value distributions: theory and applications*. World Scientific, 2000.

[30] N. M. Razali, Y. B. Wah *et al.*, "Power comparisons of Shapiro-Wilk, Kolmogorov-Smirnov, Lilliefors and Anderson-Darling tests," *Journal of statistical modeling and analytics*, vol. 2, no. 1, pp. 21–33, 2011.

[31] R. D'Agostino, *Goodness-of-Fit-techniques*. Routledge, 2017.

[32] G. Murdaca, A. Rucci, and C. Prati, "Deep learning for insar phase filtering: An optimized framework for phase unwrapping," *Remote Sensing*, vol. 14, no. 19, p. 4956, 2022.

[33] D. Marchetti, A. De Santis, S. D'Arcangelo, F. Poggio, A. Piscini, S. A. Campuzano, and W. V. De Carvalho, "Pre-earthquake chain processes detected from ground to satellite altitude in preparation of the 2016–2017 seismic sequence in central italy," *Remote Sensing of Environment*, vol. 229, pp. 93–99, 2019.

Alessio Rucci Alessio Rucci was born in Milan, Italy, in 1982. He received the M.Sc. (cum laude) and the D.Sc. degrees in electronic engineering from POLIMI, Milan, in 2007 and 2011, respectively. His thesis is on the advanced PInSAR technique and its application in reservoir monitoring and modeling. In 2008, he was with the Lawrence Berkeley National Laboratory, Berkeley, California, United States, as a Visiting Scholar to work on the InSalah Project for Carbon Capture Sequestration (CCS). In 2011, he joined the Research and Development Division of TRE, Milan, working on the assessment and estimation of atmospheric effects and surface deformation in nonurban areas.

Giovanni Costa Giovanni Costa was born in Poggiardo, Italy, in 1995. He graduated in Telecommunication Engineering with a Bachelor's Degree from Università di Pisa in July 2019 and with a Master's Degree at Politecnico di Milano in December 2021. In December 2021, he started a working experience as InSAR Processing Operator at TRE Altamira to deepen his knowledge about SAR Interferometry. In November 2022, he began as PhD fellow at Politecnico di Milano. His research focuses on signal processing techniques for space-borne synthetic aperture radar interferometry.

Andrea Virgilio Monti Guarnieri Andrea Virgilio Monti Guarnieri (Senior Member, IEEE) received the M.Sc. degree in electronic engineering (cum laude) at Politecnico di Milano in 1988. He has been a Full Professor with the Dipartimento di Elettronica, Informazione e Bioingegneria, since 2017. He is the Founder of PoliMi, spin-off Aresys, in 2003, targeting SAR, radar, and geophysics applications. He has an H index (Google) of 33, 5400 citations and holds applications for five patents. His current research interests include radar-based system design, calibration, MIMO, and geosynchronous SAR. He is a reviewer of several scientific journals and a member in scientific-technical committees of international workshops and symposia on Radar and Earth Observation (EO). He received four conference awards. He is the Guest Editor for MDPI Remote Sensing.

Marco Manzoni Marco Manzoni (Member, IEEE) was born in Lecco, Italy, in 1994. He received the B.Sc., M.Sc., and Ph.D. degrees in telecommunication engineering from the Politecnico di Milano, Milan, Italy, in 2016, 2018, and 2022, respectively. His research interests include signal processing techniques for radar remote sensing, including space-borne and car-borne synthetic aperture radar signal processing, water vapor estimation from space-borne interferometric SAR measurements, and change detection. He is currently involved in the interferometric commissioning phase of the new Copernicus Sentinel-1C mission.